Simulation of Binder Infiltration in Additive Manufacturing of Sand Molds

Patricia Erhard,* Vivek Teja Tanjavooru, Christoph Hartmann, Lucas van den Bosch, Alexander Seidel, Wolfram Volk, and Daniel Günther

This article proposes a computational fluid dynamics approach to simulate binder infiltration in 3D printing of sand molds using OpenFOAM facilitating the identification of suitable levers for application-specific material and process developments. A method for randomly generating powder bulks of designated powder size distributions (PSD) and procedures for automated analysis of the infiltration profile and volume are introduced. Simulation is utilized to investigate binder infiltration using different droplet spacings, representing different printheads' resolutions. The apparent particle size at the exact location of the droplets' impact, the droplets' landing position in relation to the respective surface topography, and thus the statistical appearance of particle formations appear to be influencing the infiltration profile. High-speed camera observations show the plausibility of the predicted infiltration kinetics. An exemplary use case compares the predicted infiltration profiles to the compressive strength of specimens printed from silica sand with low binder contents. Simulation predicts an average infiltration of 250 μm that presumably achieves reliable bonding for layer thicknesses up to 365 μm. A decrease in strength with increasing layer thickness at constant binder contents can be found in the experiment – at layer thicknesses above 350 μm, only minor strengths are achieved.

1. Introduction

Additive manufacturing (AM) technologies generate physical 3D geometries from model data using a layer-based approach.[1] AM processes commonly utilize printheads or energy beams to create and merge 2D geometries into complex 3D structures in a repetitive manner. The binder jetting process involves lowering a build platform by a preset layer thickness, filling the resulting gap between a powder dispensing unit and the build platform with powder, and the selective deposition of a bonding agent.[2]

The primary advantage of binder jetting is its high production rate and, thus, the commercial viability of large and complex parts. Nowadays, binder jetting is already utilized in the industrial series production of sand molds and cores in the casting industry. Machines realize printing volumes of up to 4 m × 2 m × 1 m.[3] An even larger 3D printer for castings up to 9.5 m in diameter is currently being developed by GE Renewable Energy, voxeljet AG, and Fraunhofer IGCV with the participation of the authors.[4]

The applied layer thickness is a decisive factor for an economic process, particularly at this size scale. Conventionally, layers of 250–350 μm are applied to fabricate casting molds and cores. Within the scope of the aforementioned project, it is intended to develop a printing strategy that allows increasing the layer thickness while keeping the binder consumption moderate.

In binder jetting technology, a binder liquid is ejected through the inkjet printheads' nozzles and penetrates the interstitial spaces within the powder. The binder is required to form capillary bridges between the particles of each layer and to bond a freshly applied layer to the previous one. The infiltration of the binder comprises an impact, spreading, wetting, and penetration phase.[5]

Understanding the binder–powder interaction and formation of binder bridges is crucial to allow for tailored process improvements. Simulations offer the prospect of decreasing experimental efforts, improving the understanding of complex relationships, and accelerating process developments.

Modeling of powder spreading via discrete-element simulations (DEM) has been conducted in various studies, focusing on investigating the impact of the particle size distributions (PSDs)[6,7] or powder spreading conditions[8] on packing density, porosity, flowability, or mechanical strength. The exact shape of the infiltrated volume depends on the binder jetting parameters and the particle structure. The infiltration shape is known to get narrower using a higher droplet ejection velocity and broader at lower powder packing densities.[9] However, a deeper understanding of the formation of binder bridges depending on the apparent packing density is crucial for applications like 3D printing of sand molds and cores. As these parts are not treated with

P. Erhard, C. Hartmann, L. van den Bosch, W. Volk, D. Günther
Fraunhofer Institute for Casting
Composite and Processing Technology IGCV
Lichtenbergstr. 15, 85748 Garching, Germany
E-mail: patricia.erhard@igcv.fraunhofer.de

V. T. Tanjavooru, A. Seidel, W. Volk
TUM School of Engineering and Design
Technical University of Munich TUM
Boltzmannstr. 15, 85748 Garching, Germany

an additional stabilizing postprocessing step like sintering or hot isostatic pressing, the binder bridges determine the final overall strength of the respective mold or core.

Numerical modeling of the penetration of droplets into porous media is increasingly being investigated by applying simplified computational fluid dynamics (CFD) models. Wang et al. developed a 2D simulation using COMSOL Multiphysics software and studied the influences of contact angle, porosity, and droplet ejection height on the penetrated area.[9] Gao et al. suggested a cylindrical penetration model for multilayer simulation using COMSOL.[10] Deng et al. studied the kinetics of micrometer-sized droplets and their influence on lateral spreading and infiltration.[11] Colton and Crane were able to show that the droplet velocity, spacing, and interarrival time have a significant impact on the effective saturation and the successful line formation.[12] Fu et al. studied the effects of droplet characteristics on spreading and penetration inside a thick porous substrate by use of Ansys Fluent and found a crucial influence of the ratio between droplet and particle diameter on the droplet dynamics.[13] Similarly, Li et al. found the spreading of microdroplets propagating completely different at droplet–powder diameter ratios <1 and highlighted the need for investigations of the spreading behavior explicitly with regard to particle sizes larger than the droplet sizes in 3D printing.[14] Tan proposed a 3D numerical method to investigate the impact of micrometer-sized droplets on a powder bed.[15] Wagner et al. presented a similar simulation setup but a polydispersed random packing arrangement.[16] The small droplets in inkjet printing make dynamic studies of droplet infiltration challenging.[17] Experimental studies generally investigate binder infiltration on larger droplet sizes[18] due to the simpler observation of the infiltration with optical methods. To allow for obtaining subsurface information with high spatial and temporal resolution, Parab et al. used a high-speed synchrotron X-ray imaging technique to observe the binder jetting process in real time.[19] Rehman et al. developed a computational model for binder jetting that combines CFD and DEM and found a higher binder penetration depth in the droplet impact area. This effect is attributed to decreasing capillary forces over time.[20]

Particularly in this respect, it is important to discuss the nature of sand binder jetting compared to metal binder jetting which is the focus of the published literature. The saturation in sand printing is well below 10% and the mean powder particle diameter significantly larger than the droplet diameter. On this account, the impact phase is expected to take a more dominant role in sand infiltration while the capillary forces have been revealed crucial in aforementioned examinations dealing with smaller solid particles sizes than droplet sizes as it is typical in, for example, binder jetting of stainless steel 316L.[20] Little literature is available on powder–binder interaction during 3D printing of sand. Cheng et al. studied the infiltration of furfuryl alcohol in sand with a custom 3D printing machine. Using a grayscale printhead, they found the dimensional error, and strength can be optimized using different droplet sizes.[21] Hartmann et al. demonstrated how an understanding of the liquid spreading can help to control the infiltration depth using different droplet sizes in a greyscale printhead. With this approach, a near-net-shape geometry without stair steps could be demonstrated.[22] To the knowledge of the authors, there exists no prior study that focuses on the 3D infiltration of different

droplet patterns at a size scale present in industrial sand inkjet printing while implementing random packings that are realistically reproduced from spheres according to their PSD.

This work presents a CFD approach to simulate the binder infiltration within the OpenFOAM environment, version v1912.[23] A simulation tool is developed to investigate binder distribution within powder beds constituted from designated PSDs along with appropriate image processing methods.

This tool aims to facilitate the creation of an advanced process understanding of powder–binder interaction as an alternative or complementary approach to experiments during application-specific process developments. As an exemplary use case, the influence of the location of droplet impact on the infiltration profile in large-format 3D sand printing is investigated. A silica sand and furan binder system, both typical for use in 3D-printed sand molds for the foundry industry, is utilized. By experiment, different droplet arrangements (2D droplet spacings, representing different printheads and resolution parameters) are investigated for their infiltration behavior by varying an inkjet printhead's resolution in two directions. Specimens of different layer thicknesses are fabricated. The printing pattern's influence on the binder infiltration is examined by evaluating the 3D infiltration shape and depth using simulation. The measurements are put into context with compressive strengths attained in experiments. This article proposes a CFD approach and post-processing analysis methods to predict the infiltration behavior that may create the basis for fast material qualifications and optimization in resource-efficient process control in binder jetting and shows an exemplary use case for a first study on the effect of the droplet impact location on the infiltration profile in 3D sand printing.

2. Experimental Section

2.1. Raw Materials

The powder material selected for this study was the commercially available silica sand GS14 RP (Strobel Quarzsand GmbH, Freihung, Germany). It shows a medium grain size of 135 µm and a high degree of uniformity. Approximately 90 wt% of the grains show a size within the range between 2/3 and 4/3 of the medium grain size.[24]

The two-component binder system VX-2C Typ B (voxeljet AG, Friedberg, Germany) comprise a reactive furan resin, consisting of mainly furfuryl alcohol, processed in the inkjet printhead, and an acid catalyst based on p-Toluenesulfonic acid. This catalyst is often referred to as activator fluid. The powder was premixed with 0.3 wt % of acid catalyst in a household mixing apparatus for 10 min.

The fluid properties (**Table 1**) were determined experimentally using the optical contact angle goniometer and drop-shape analysis system OCA 25 (DataPhysics Instruments GmbH,

Table 1. Fluid properties at 20 °C.

Fluid	Density in g cm^{-3}	Kinematic viscosity in mPa s	Contact angle in °	Surface tension in mN m^{-1}
Binder	1.1	7.5	33.5	38.4
Activator	1.2	15	13.5	46.5

Filderstadt, Germany) and the viscosimeter MCR 302 (Anton Paar AG, Graz, Austria). The substrate for the contact angle measurement was a commercial quartz glass plate. The surface was cleaned, but remained untreated otherwise.

2.2. Setup for High-Speed Camera Observation of Binder Infiltration

An experiment high-speed camera setup was used for model testing. For this purpose, a Phantom v2640 (Vision Research, Inc., Wayne, NJ, USA) was deployed in the printer. A macrofixed focal length lenses with a focal length $f = 100\,mm$ was used in combination with a Laowa 100 mm f/2.8 2× Macro APO (Venus Optics, Hefei, China).
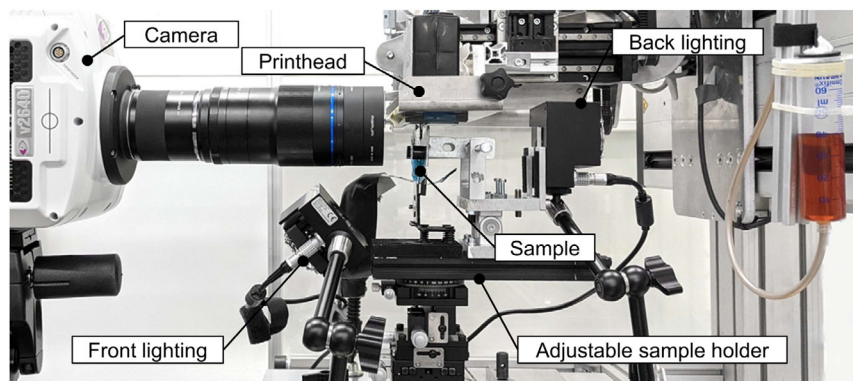
Figure 1 shows the setup for high-speed observation of binder infiltration. A glued sample package of two cover glasses with a paper spacer was inserted into an adjustable sample holder. Between these two glass plates, grains of sand of GS14 RP sand were manually inserted from above until they were packed as close as possible to each other. The result was a thin arrangement of individual grains of sand with a thickness of $\approx 0.2\,mm$ that must not be larger due to the requirement of transparency defined by the camera setup. The vibration of the printer during printing did not allow a dynamic measurement, so a static setup was prepared in which a row of nozzles of the printhead was positioned exactly above the 0.2 mm gap. Due to the nozzle spacing of 508 µm in the printhead, a realistic drop spacing cannot be realized. For this reason, a single nozzle was triggered eight times at a frequency of 1575 Hz in the same position to collect an accumulated volume of furan resin of $\approx 1\,\mu g$ or 950 pl between the particles, which was of a comparable magnitude with the volume dispersed in the simulation study but not distributed equally.

Using this setup, the infiltration kinetics or the infiltration progress over time was observed as realistic as possible to test the simulation model's plausibility. To be able to receive an informative image displaying the intensity of change, a combination of front and back lighting was used. The images shown were difference images. Each image was aligned with half-pixel accuracy to a common early reference frame containing sand particles without any droplets. Then, each image was converted to the difference representation relative to the reference frame, which highlights the added binder fluid, barring small alignment errors in the static sand packing. Finally, all images were inverted and increased in contrast for better visualization.

2.3. 3D Printing Test Setup

The binder jetting process was realized in a fully automated test setup (**Figure 2**) by applying the following process steps iteratively until the desired build height was reached: 1) adjustment

Figure 1. Setup for high-speed observation of binder infiltration.
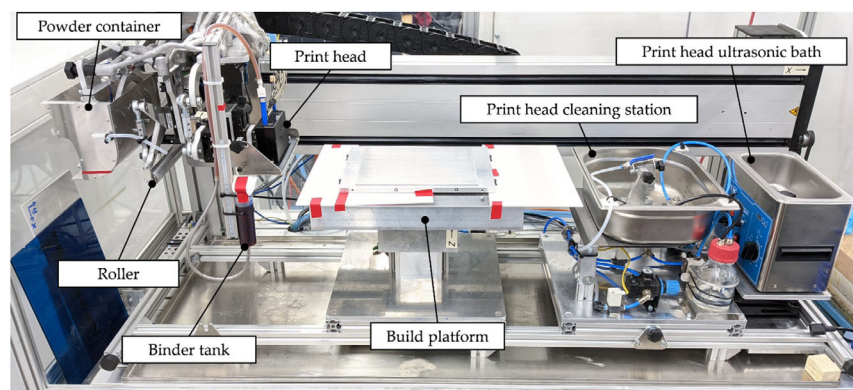
Figure 2. Binder jetting test setup. Reproduced under terms of the CC-BY license.[22] Copyright 2022, Hartmann et al.

of the build platform to the desired layer thickness; 2) deposition of a powder layer; 3) lowering of the build platform; and 4) printing onto the layer.

The utilized printhead (Dimatix StarFire SG1024 1C MC LA, Fujifilm Dimatix, Inc., Santa Clara, USA) comprised 1024 nozzles distributed over eight rows and supported 2-bit grayscale printing at 400 dpi resolution and droplet deposition timing via a linear encoder. The print speed was set to $100 \, \mathrm{mm \, s^{-1}}$, and the distance between the printhead and powder bed was set to 5 mm. A pulse of 5 μm pulse width was set, yielding a total droplet mass of 37 ng per nozzle actuation. The droplet mass was determined by printing five images of 1024×1024 pixels onto an artificial sand bed attached to an electronic scale with a resolution of 0.001 g. The weight measurement was repeated four times. The droplet mass of 37 ng corresponded to the average of these measurements (deviation $< \pm 0.3\%$). The bitmaps of the print were created manually using the software GIMP 2.10.[25] The average droplet speed was measured to be $3.6 \, \mathrm{m \, s^{-1}}$ by high-speed camera observations using a Phantom v2640. For every single-electric actuation, one droplet pair was ejected. The resulting frequency as a consequence of print speed and set resolution was estimated to 1575 Hz. This led to an interarrival time of droplets of 0.635 ms. Due to the small width of the print image, one layer was completed with a single pass of the printhead. The process was carried out at $22 \pm 2 \,°\mathrm{C}$ with $23 \pm 5\%$ relative humidity (hereinafter referred to as ambient conditions).

2.4. Experimental Matrix

An exemplary use case was defined for a first study on the effectiveness of the simulation and analysis tools for problem solving during binder jetting process developments. Droplet spacing or resolution in x- and y-plane ($\mathrm{res}_x, \mathrm{res}_y$) is an essential characteristic in binder jetting that is, depending on the printhead used, either fixed by machine technology constraints or variable by the operator to a certain extent. In contrast to the fluid parameters like droplet size, droplet viscosity, or the binder's rheological properties that are equally important in binder jetting but mutually interacting, droplet spacing does not affect the characteristics of fluid ejection. It was thus defined as the parameter for applying the simulation approach for the first time. Thereby it was determined whether varying the location of droplet impact enables exerting influence on the infiltration profile in 3D sand printing.

The 3D printing setup allowed tailoring the droplet spacing in the x–y-plane. The printhead's theoretical hardware resolution (63.75 μm in x and y) was kept constant throughout the experiments while the slicing data was modified to allow for depositing only every second droplet pair, which equaled software-controlled resolution of 127.5 μm (droplet pattern no. 2), every third (191.25 μm, droplet pattern no. 1), or every fourth droplet pair (255 μm, droplet pattern no. 3) (**Table 2**). The ejected binder volume, which is decisive for overall strength, was kept at similar levels by aligning the resolutions in x and y. The powder bed density δ_{bulk} using the test setup and material system described above was determined to be $\approx 1.35 \, \mathrm{g \, cm^{-3}}$ (deviation $< \pm 5\%$) and resulted in a packing fraction of $\approx 50.9\%$. A variance in powder bed density when altering the layer thickness was neglected

when calculating the binder content c in relation to the sand weight.

Table 2 summarizes the parameter sets investigated in the main part of this study and the respective representative volume element (RVE) sizes relevant to the simulation setup. Patterns no. 1 and no. 3 represented stripe-like patterns with full resolution in one direction and two (no. 1) or three pixels spacings (no. 3) between the droplets. No. 2 showed an equal droplet distribution in the plane using only every second nozzle available and printing only every second pixel. Although the printhead utilized herein allows for printing any desired pattern, doubly symmetrical patterns were chosen due to their easy implementation in any binder jetting machine. By alternating the respective direction of the stripes (a vs. b) in no. 1 and no. 3, an influence of the recoating process on the experimental results that cannot be represented in the simulation was investigated. The recoater moved along the y-axis. Accordingly, pattern a was striped perpendicularly to the recoating direction and b parallel. Three different layer thicknesses or resolutions in z-direction res_z were used: 350 μm as the common standard in processing GS14 RP sand, as well as two significantly higher values of 470 and 510 μm, leading to decreased binder contents when printing with the same resolution. The total droplet mass m_{droplet} of 37 ng was kept constant throughout the main study. The density of furan resin was determined gravimetrically by means of a defined volume of 100 mL to be $1.1 \, \mathrm{g \, cm^{-3}}$ (deviation $< \pm 8\%$).

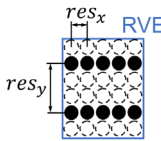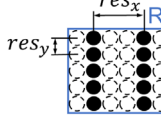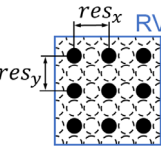The resulting calculated binder contents c are additionally listed in Table 2. Those are calculated as follows
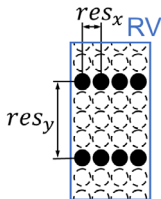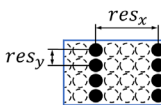
$$c = \frac{m_{\mathrm{droplet}}}{\mathrm{res}_x \cdot \mathrm{res}_y \cdot \mathrm{res}_z \cdot \delta_{\mathrm{bulk}}} \quad (1)$$

The saturation was estimated using experimentally validated fluid densities and packing fractions. Knowing the added catalyst mass and the described droplet mass, the liquid volume can be calculated using the fluid densities. After printing, each sample was measured and the void volume between the sand grains was derived from its printed dimensions, weight, and sand mass after burnout. The saturation was the ratio between the fluid volume and the void volume. To enable comparability, the parameters were carefully chosen to set up the calculated binder content to 0.48 wt% in at least one of the experiments of each droplet pattern.

A preliminary experimental study was carried out considering an enlarged range of binder content (until 1.5 wt%, which is the typical upper limit for industrial use of furan binder in binder jetting of sand molds) for the chosen levels of layer thickness by properly adjusting the droplet sizes to 37, 85, and 131 ng using the procedure described above and utilizing the printing patterns listed in Table 2, first column. The preliminary experiment was, unlike the main experiment, not accompanied by simulation runs. It was used to define the experiment design by enabling the selection of parameters for specimens showing low but measurable strength values in accordance with the intended determination of binder-saving printing strategies. Moreover, by exploiting the enlarged ranges of binder content, the motivation behind the overarching research issue in binder jetting, the declining structural integrity with higher layer thicknesses at equal binder contents, was illustrated and quantified in terms of the property of compressive strength.

Table 2. Experimental matrix.

Droplet pattern	Resolution x res_x in μm	Resolution y res_y in μm	Layer thickness res_z in μm	Binder content c in wt%	Saturation S in %	Size of RVE in x and y in μm × μm
No. 1a	63.75	191.25	350	0.64	1.51	318.75 × 382.5
	63.75	191.25	470	0.48	1.13	
	63.75	191.25	510	0.44	1.04	
No. 1b	191.25	63.75	350	0.64	1.51	382.5 × 318.75
	191.25	63.75	470	0.48	1.13	
	191.25	63.75	510	0.44	1.04	
No. 2	127.5	127.5	350	0.48	1.13	382.5 × 382.5
	127.5	127.5	470	0.36	0.85	
	127.5	127.5	510	0.33	0.78	
No. 3a	63.75	255	350	0.48	1.13	255 × 510
	63.75	255	470	0.36	0.85	
	63.75	255	510	0.33	0.78	
No. 3b	255	63.75	350	0.48	1.13	510 × 255
	255	63.75	470	0.36	0.85	
	255	63.75	510	0.33	0.78	

Furan binder systems polymerize by polycondensation under the release of water and show a strength propagation over time.[26] The time for curing was set to 24 h at ambient conditions to allow for comparable strength development of all specimens fabricated up to the time of analysis. Five specimens of each parameter combination ($n = 5$) were fabricated to account for statistical variations in experimental runs. In terms of simulation, the printing patterns no. 1, no. 2, and no. 3 are applied on three different powder bulk RVEs, showing comparable packing fractions but different particle arrangements.

2.5. Sample Geometry and Printing Position

Cuboids with the size of 30 mm × 30 mm × 10 mm ($x \times y \times z$) were printed. All specimens were positioned randomly within the building volume with at least 3 mm of clearance (10 mm in x, 10 mm in y, and 3 mm in z) (**Figure 3**).

2.6. Material Characterization

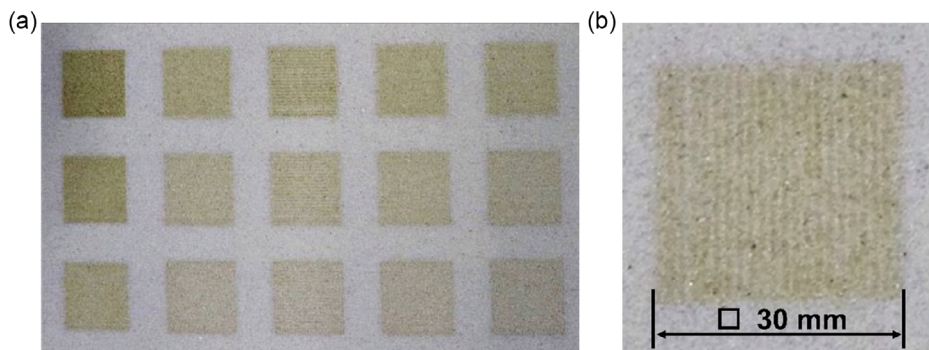Compression testing was conducted on the universal testing machine Z020 (ZwickRoell GmbH & Co. KG, Ulm, Germany) using a 20 kN load cell. A preload of 1 N and a testing speed of 0.7 mm min^{-1} were set.

3. Numerical Modeling

Multiphase flow was modeled in OpenFOAM using the solver interFoam, which applies the volume-of-fluid (VOF) method together with the continuum-surface-force (CSF) method for the determination of the phase interfaces for incompressible, immiscible fluids.[27] It involves the inclusion of an additional term for the volume fraction in the conventional Navier–Stokes equation. VOF and CSF methods for multiphase flow modeling were intensively described in the literature, for example, Brackbill et al.[28] and Nieves-Remacha et al.[29] One advantage of the VOF method is the possibility of modeling breakup and coalescence.[30]

3.1. Definition of the RVE

RVE is the minimum volume that accurately represents the characteristics of the whole system during a measurement or simulation.[31] The RVE should be large enough to statistically map all microstructural heterogeneities that occur in the material.[32]

**ADVANCED
SCIENCE NEWS**
www.advancedsciencenews.com

**ADVANCED
ENGINEERING
MATERIALS**
www.aem-journal.com

Figure 3. a) Randomized positioning of specimens with different droplet patterns within the building volume. b) Detailed view on the cross section of one cuboid printed with droplet pattern no. 3.

When translated into binder jetting technology, the concept of RVE implies the volume of the sand layer considered to study the infiltration of one binder droplet or a matrix of droplets. These infiltration results can then be scaled up by multiplying them with the total number of such RVE volumes present in the sand layer to obtain an approximate representation of infiltration in the entire layer. Hence, from a simulation standpoint, the results from one RVE of the sand layer can be used to estimate the infiltration in the entire layer. Ideally, increasing the RVE volume (and also the matrix of droplets) leads to more accurate statistics when scaled up to the entire layer volume and vice versa. At the same time, a larger RVE requires a larger simulation space which in turn is proportional to the number of cells of the CFD mesh. Therefore, the simulation time is directly proportional to the size of the RVE if the resolution of the CFD mesh is kept constant. Table 2 gives the sizes of the RVEs chosen in this study in x and y. Those are a multiplication of the respective resolution by the number of droplet pairs ejected in this dimension. This is to ensure that not the boundary regions of a printed cross section within a layer are monitored in the simulation but the inside area that is surrounded by similar RVEs in the actual setup. The size of the RVE in z was set to 510 μm, which was the maximum layer thickness applied in the experiments. Since each binder bridge connects two or more grains that may not otherwise be bonded, infiltration of the entire RVE means that sufficient bonding is assumed for a layer thickness equal to the height of the RVE. It cannot be guaranteed that the chosen RVE sizes accurately represented all microstructural details that determine the macroscopic behavior of the sand layer. Though, using three different, randomly generated RVEs of the same outer dimensions, information on this was provided during the study itself. Each pair of droplets ejected at distinct locations in the experiment was aggregated into one droplet with a total droplet mass of 37 ng for simplification purposes in the simulation. Prior to binder ejection, an acid catalyst (activator fluid) was dispensed to the powder bulk (Figure 6). The fluid proportion was set equal to the 0.3 wt% of the powder bulk apparent in the experiments.

3.2. Powder Packing Algorithm

A sequential addition packing algorithm developed by Zhou et al.[33] was adopted to model the packed sand structure of desired packing fractions inside the powder bed.

To initiate packing, a PSD was prescribed from which a sphere was randomly selected and dropped into a rectangular container. The subsequently inserted spheres were positioned via dropping and rolling rules. The spheres' gravitational potential within the container was minimized when brought in their final position. The algorithm built up the particle structure from a plane base. Since the recoater straightened the powder bulk along the roller's line of contact, the particle structure was rotated by 180° to take this effect into account. The rigid wall effects of the container were eliminated using a periodic boundary to allow the portion of spherical particles which leave a face or corner of the container to re-enter into it from the opposite face or corner respectively.[33] The algorithm was implemented in GNU Octave (version 6.1.0),[34] which generated a data file and a visual representation of the microstructure. The coordinates of the final positions of the centers of each particle were saved in this data file. This further acted as an input to develop an STL file using an open-source finite element mesh generator called Gmsh[35] with built-in support for constructive solid geometry (CSG) to create object surfaces. After the algorithm finished building up the powder bulk, no further powder movement was allowed in the situation. Experimental high-speed camera observations confirmed that there was no relevant movement of sand grains during printing (Figure 10). Thus, the solid particle material was assumed to be fixed. All particles within the RVE were treated as one solid bulk and couldn't move toward each other in the static model (**Figure 4**).

The STL generation via the powder packing algorithm was repeated until the desired bulk density of 1.35 g cm^{-3} was reached at a tolerance of ±5%, resulting in a packing fraction of ≈50.9%, following the experimental data of the recoating setup utilized. To investigate the influence of the powder arrangement on binder infiltration, three powder RVEs were generated using this procedure for each simulation case that corresponded to one droplet pattern.

3.3. Meshing

OpenFOAM meshing utilities were used to discretize the simulation domain. This discretization was carried out in three steps using three utilities of OpenFOAM meshing: blockMesh, surfaceFeatureExtract, and snappyHexMesh. The blockMesh utility creates a background mesh enclosing the
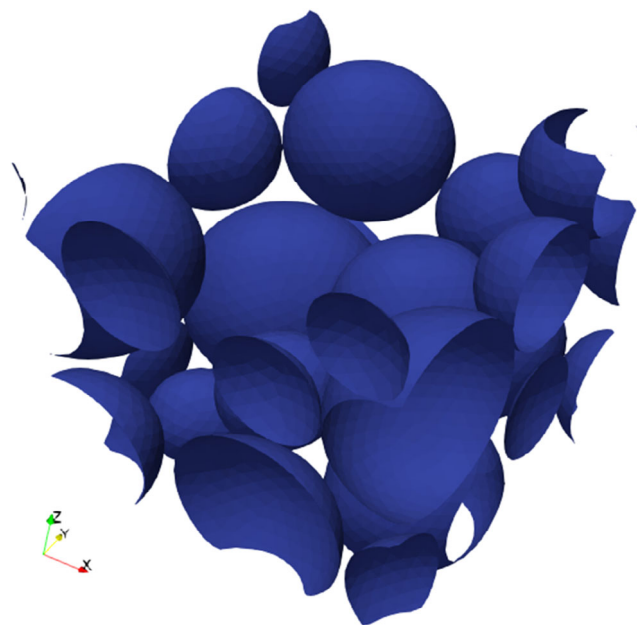
Figure 4. Microstructure STL file generated from Gmsh.

overall simulation domain. The features of the geometry's surface are extracted by the surfaceFeatureExtract utility. snappyHexMesh refines the mesh, removes the cells from the spheres' insides, and snaps the remaining cell nodes.[27] The resulting mesh was a complex combination of structured and unstructured grids around the particle geometry (**Figure 5**).

3.4. Boundary Conditions

The boundary conditions of the CFD domain are shown in **Figure 6**. There, each boundary face is depicted, and the type of boundary condition, as well as its relationship with other patches, is showcased. The left, right, front, and back boundaries were modeled with a cyclic boundary condition to imitate the effect of four neighboring microstructures interacting with the one being simulated. This means that if binder exits the domain on one side, it re-enters the domain on the opposite side, defined as the neighbourPatch.

The boundary condition inletOutlet for α was used, providing a generic outflow condition that allowed for the binder to exit the domain at the outlet patch, and a specified inflow[27] that was set to 0, meaning that exclusively air was allowed to re-enter the domain through the inlet patch. The boundary conditions were defined as described for the three process parameters of interest, the fluid fraction α, the static pressure without hydrostatic contribution p_{rgh}, and the velocity U. The droplets were introduced in the simulation as an initial condition for α and U in a predefined region. Within this region, α was set to 1 (each element was fully filled with liquid), and U is set to (0 0 u_init), with u_init being the initial droplet velocity in the z-direction. In the rest of the domain, α, p_{rgh}, and U were set to 0.

3.5. Simulation Parameters

Resin droplets were modeled according to their position in the RVE. From the experimentally determined droplet mass and the fluid density, a single-droplet diameter of 40 µm was determined. The measured droplet velocity was assigned to each droplet as described earlier. Binder impact and spreading are known to occur within microseconds due to their kinetic energy. Further permeation is driven by capillary forces dependent on the powder structure and liquid proportion.[5] Gravity is negligible because of the low mass of the droplets.[36,37] The gel time of furan resins is in the order of minutes[38] and was thus expected not to influence the binder infiltration behavior as it was investigated herein. The simulation time was set to 0.6 s.

Each droplet pattern was simulated in combination with three different RVEs that showed a similar packing fraction but different particle arrangements (simulation 1.1, 1.2, and 1.3 for pattern no. 1, simulation 2.1, 2.2, and 2.3 for pattern no. 2, and simulation 3.1, 3.2, and 3.3 for pattern no. 3).

(a)   (b)
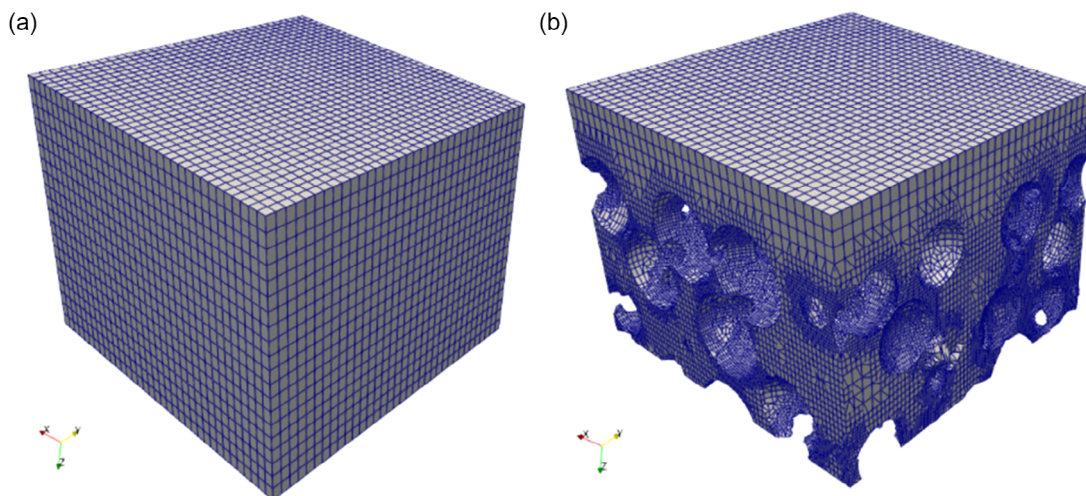
Figure 5. a) Background mesh from blockMesh and b) final mesh from snappyHexMesh.

2300212 (7 of 20)
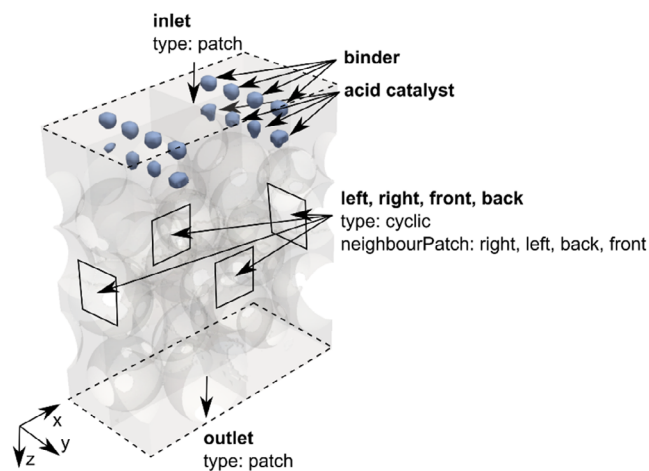
Figure 6. Depiction of the simulation environment on the example of droplet pattern no. 3 at $t = 0\,\mu s$.

3.6. Postprocessing

ParaView version 5.9.0 (Kitware, Clifton Park, NY, USA)[39] was used to visualize the results. An automation code was developed in this work to postprocess the results of these simulations. To visualize the simulation of binder into a rigid porous microstructure, the interface between the liquid binder and air was tracked via the contour filter of ParaView. This filter can differentiate the zone occupied by the binder by creating an isosurface which is the volume fraction of the binder in each cell as per the theory of the VOF method. An isosurface value of $\alpha = 0.5$ was considered to visualize the binder movement during its ejection and infiltration. **Figure 7** illustrates the application of the post-processing tool for a single-droplet infiltration scenario. While Figure 7a, b shows the single-droplet ejection and infiltration at the end of an exemplary simulation, Figure 7c shows an instance of the automated slice filter of ParaView extracting infiltration data at desired intervals along the depth of the microstructure.

The infiltration of the binder inside the microstructure was studied. The values of the infiltration depth determined by the respective slice and the binder spreading along the x- and y-directions in the form of the x- and y-range within each slice were of utmost interest and extracted from the simulation results by identifying the location of fluid proportions via VOF at certain timesteps.

The postprocessing data analysis tool uses the Python interface of ParaView to calculate the infiltration depth and the maximum extent of spreading of the binder fluid inside the microstructure in the x- and y-direction applying a slicing approach. Volume elements were calculated by multiplying the respective delta value of each minimum and maximum extension in x- and y-direction (a cuboidal outline of the respective area occupied by a fluid) and the interval depth of $2\,\mu m$. They defined the maximum volume of spreading in a predefined layer to analyze the binder distribution in the overall microstructure and were set in relation to the powder packing to calculate an approximated proportion of infiltrated binder volume in the z-direction. Moreover, the minimum and maximum coordinate positions of the binder in each data layer were analyzed. Thereby, the outline of the infiltration pattern was plotted. This postprocessing strategy was a first approach to automized analysis, aiming for easier interpretability. An upcoming version of the tool may enable exact localization of binder volume in each slice and generation of a 3D geometry from those allowing to superimpose the binder proportion and the powder packing.

4. Verification Approach by Benchmarking a Single Droplet Infiltration Case

The OpenFOAM simulation developed in this work was compared with the Gerris simulation demonstrated by Tan.[15] For simplicity, the Gerris simulation considered a uniform particle size of $20\,\mu m$ throughout the microstructure. The simulation was carried out for a time of $50\,\mu s$ to analyze the effects of the impact of a single droplet on a face-centered-cubic (FCC) arranged microstructure of size $100\,\mu m \times 100\,\mu m \times 65\,\mu m$, as shown in **Figure 8**a. Figure 8b showcases the OpenFOAM simulation modeled similar to the Gerris simulation with a uniform particle diameter of $20\,\mu m$ and a packing fraction of 48.7%.

The physical model of the sand microstructure is different with respect to the meshing (Gerris: adaptive mesh refinement, here: static meshing) and particle packing. The Gerris simulation
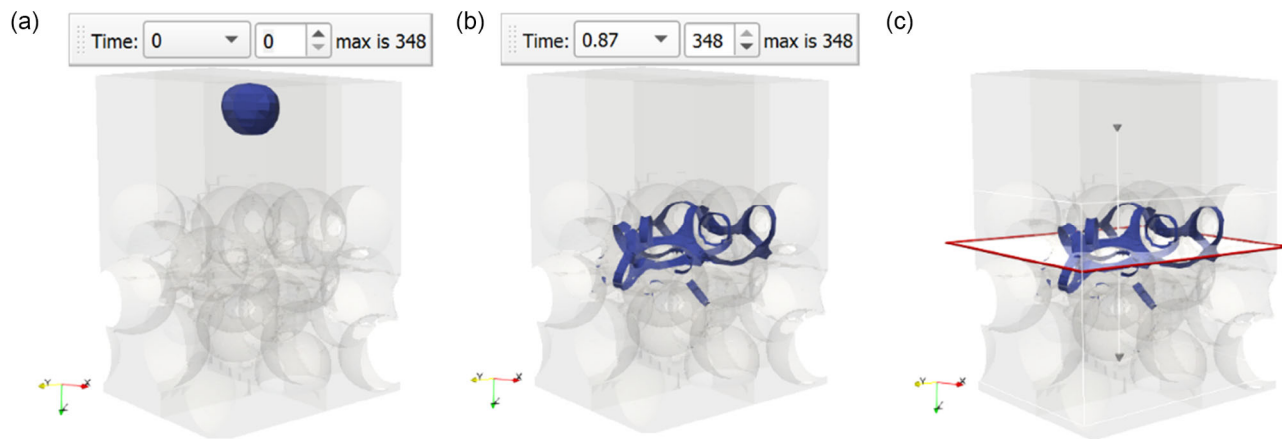
Figure 7. a) Ejection of binder droplet at $t = 0\,\mu s$, b) infiltrated microstructure at $t = 0.87\,s$, and c) data acquisition using slice and contour filter.

ADVANCED
SCIENCE NEWS
www.advancedsciencenews.com

ADVANCED
ENGINEERING
MATERIALS
www.aem-journal.com

uses an FCC packing, whereas the OpenFOAM simulation in this work uses a sequential addition packing algorithm. The irregular arrangement in this work had the same packing fraction. An implementation of FCC packing in OpenFOAM is renounced even though it may provide a more significant verification. Instead, the importance of the particle arrangement was demonstrated. In **Figure 9**, the droplet infiltration into the microstructure at different timesteps is displayed. At 4 μs, the droplet contacts the powder. Already 4 μs later, the droplet is spread in a circle around the location of droplet impact. The particles' surfaces are covered with fluid but become successively uncovered as the fluid infiltrates the powder bulk. At the end of 50 μs, in the case of the Gerris simulation, the infiltration depth was 35 μm, and the infiltration diameter was 56 μm (dashed circle). On the other hand, for the simulation using OpenFOAM with a microstructure of the same packing fraction, the depth of infiltration was 36 μm, and the diameter of infiltration was determined to be roughly 65 μm using the image processing software ImageJ[40] and maximum 80 μm using the automated analysis introduced above. The infiltration depth attained is almost equal. However, there was a major difference in the value of infiltration diameter. The difference in the infiltrated volume is assumed to be largely due to the different microstructure models used. While Tan's FCC packing showed a minimum distance of 3 μm between the particles, the packing algorithm implemented herein[33] created touching spheres and, thus, narrower capillary channels as well as irregularly large gaps or flow resistances. There is established research that the porosity of the microstructure is an influential factor for infiltration,[5] which was confirmed here.

To sum it up, the simulation setup presented herein shows comprehensible results and generates infiltration profiles that lie in the same magnitude as the Gerris simulation.

5. Results and Discussions

This section first introduces results. Second, the respective simulation data are examined by infiltration analysis. Finally, the experimental and simulation results are compared and discussed.

5.1. Results

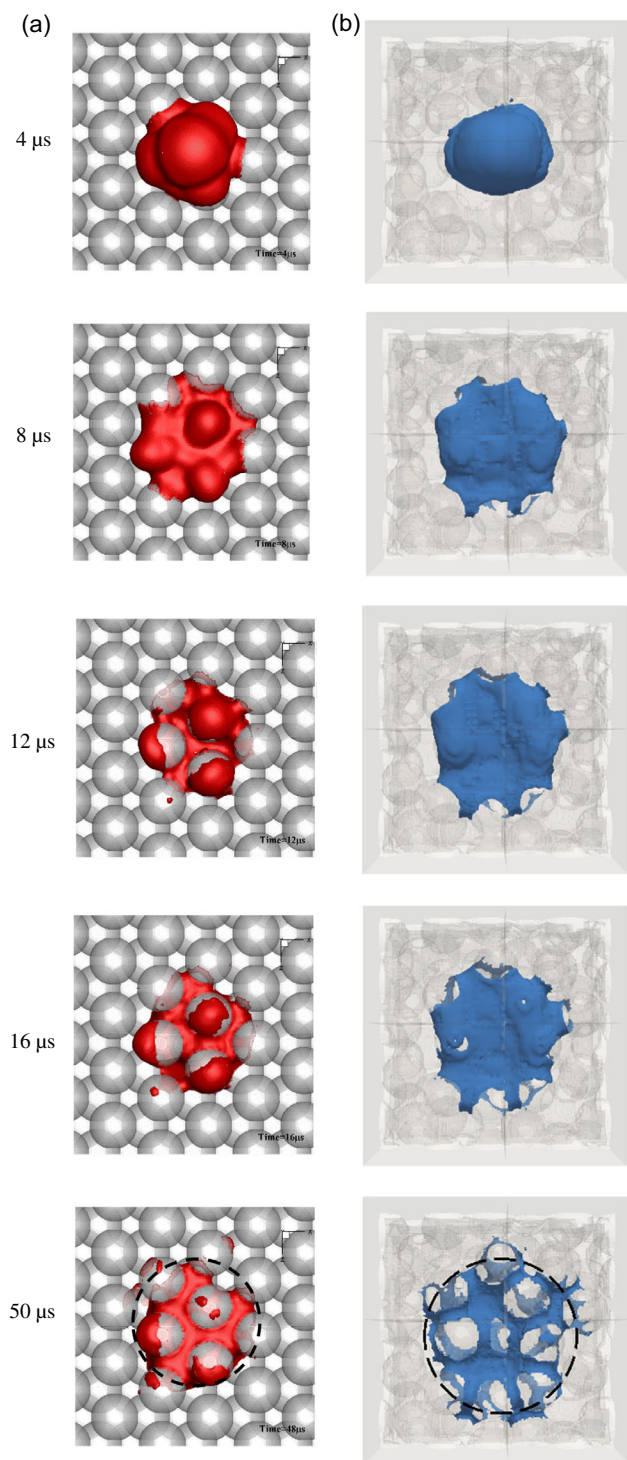#### 5.1.1. Observation of the Infiltration Kinetics

Investigations on the process of infiltration of droplets of the small droplet sizes (in the range of pl) in real powder bulks within experimental setups are highly challenging due to the requirements with respect to the small droplet size and observation space and the dynamics of the infiltration process. It has to be noted that due to those restrictions given by the hardware setup and optical mode of observation, no droplet patterns can be mapped but multiple droplets deposited on the same location. By observing the infiltration of eight sucessive droplets deposited on a powder stacking of sand, the kinetics of the infiltration process were investigated. This enables the testing of the simulation model in terms of the infiltration kinematics.

Figure 10 shows the chronological sequence during infiltration of the binder droplets on an exemplary powder stacking of sand GS14 RP using the setup for high-speed camera observation as introduced in 2.2.1. In this example, most of the infiltration is observed within the first 20 ms. Binder is shown to overcome the grain that is subject to binder impact and a second grain in all directions in that short time. At 250 ms, the binder propagates to another sand grain. Then no further infiltration is apparent until 1 s.

The new observation approach is regarded as appropriate for investigating the infiltration kinetics of multiple droplets ejected by an industrial inkjet printhead in a sand stacking enabling the approximation of estimated infiltration time and area. However, it has to be noted that even the advanced real-time observation as proposed herein demands for thin observation volumes and sufficient fluid volume to be tracked and is thus afflicted with errors. Moreover, the high light exposure necessary for sufficient contrast may heat
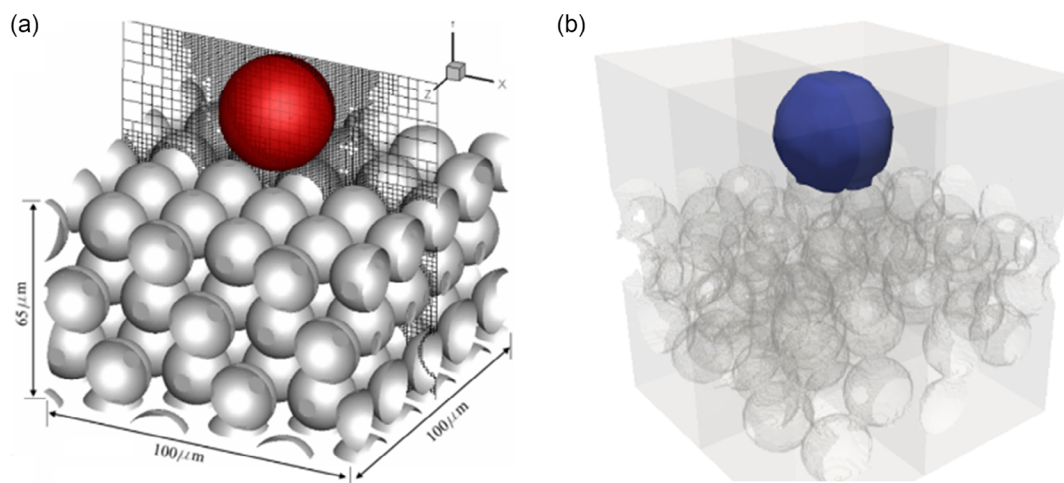
Figure 8. Simulation at $t = 0\,\mu s$. a) Gerris Simulation. Reproduced with permission.[15] Copyright 2016, Elsevier Chemical Engineering Science. b) OpenFOAM simulation.

**ADVANCED
SCIENCE NEWS**

www.advancedsciencenews.com

**ADVANCED
ENGINEERING
MATERIALS**

www.aem-journal.com

Figure 9. Top view on droplet impact at different timesteps. The dashed circle at $t = 50 \mu s$ visualizes the infiltration diameter. a) Gerris Simulation. Reproduced with permission.[15] Copyright 2016, Elsevier Chemical Engineering Science. b) OpenFOAM simulation.

up the system, or binder fluid may make contact with the glass walls during infiltration. Those conditions may distort the results.

5.1.2. Compression Strength Testing

The fundamental challenge with high layer thicknesses desirable for economic reasons in several operations is illustrated in **Figure 11**. It shows the relation between the binder content and the compressive strength of specimens. The range of the binder content is comparable to what is common in industrial binder jetting of sand molds. As shown, the compressive strength increases with growing binder contents. Since the organic bonds are the weakest links, fracture occurs between the particles. Stronger individual bonds and a higher number of binder bridges consequently lead to a higher resistance to fracture within a green body.[41,42]

Figure 11 demonstrates that higher layer thicknesses result in lower strength values for the same binder content. One can argue that improved compaction and higher packing densities in 3D printing are typically achievable at a lower layer thickness.[43] Though no measurable differentiation in density was detected in this study. The decrease in strength with increasing layer thickness at a constant binder content is consistent with results from the literature, for example, Vaezi and Chua.[44]

The organic binder system is a wetting liquid pulled into the neck regions by capillary action. However, the authors' hypothesis states that the capillary forces are too low to enable the liquid to overcome longer distances due to a high probability of coming across a random local discontinuity that offers an energetically more favorable condition for settlement than flowing, for example, macrovoids that are known to inhibit liquid flow in irregular packed powders.[45] To apply thick layers quickly as well as to use binder efficiently is a typical scope in current machine and process developments. This question could be researched in the future with the methods presented herein.

Figure 12 shows the results of compressive strength testing, following the categorization according to the droplet spacing, as defined in Table 2.

Each level of layer thickness allows the same observation: The specimens printed with the droplet pattern no. 1b or 3b (representing patterns striped parallel to the recoating direction) show a consistently and significantly higher strength compared to no. 1a or 3a (representing the droplet patterns striped perpendicular to the recoating direction). Specimens printed with a uniform pattern show a comparable strength like the patterns striped in the recoating direction for the same binder content.

Figure 13 visualizes the dependency of strength on droplet spacing as a function of binder content for binder contents below 0.5%. For the value range displayed, a roughly exponential course in strength development is apparent. This behavior has also been observed in other studies[42,46] and was incorporated in a later model approach[42] based on the beforementioned theoretical description.[41]

The binder content of 0.33% is the minimum amount of binder necessary to fabricate specimens stable enough for a manual and cautious excavation from the powder bed. No clear distinction between the specimens of different printing patterns can be made at this level. With increasing binder content, those fabrication series show an increasingly diverging trend.
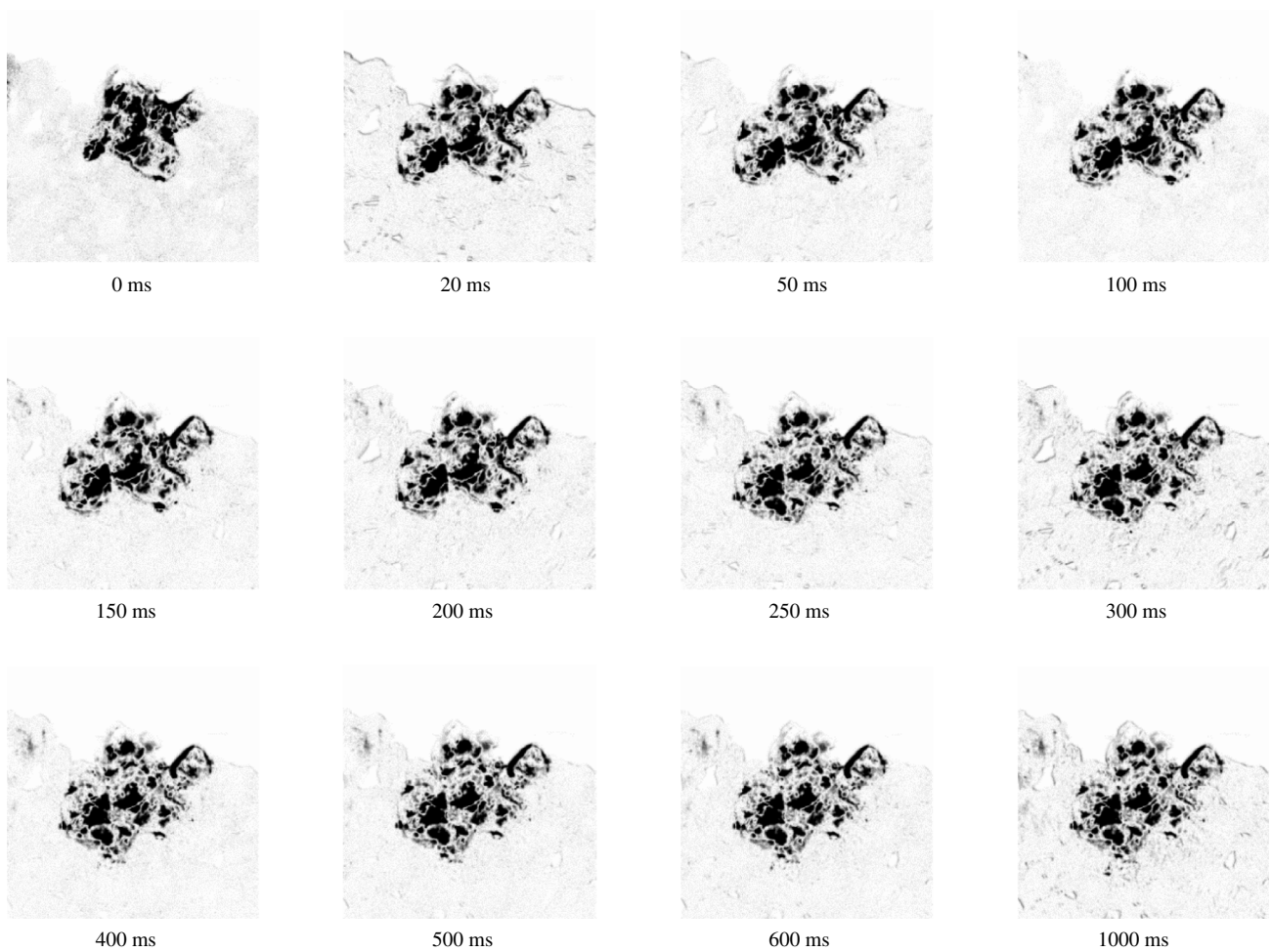
Figure 10. Chronological sequence of the infiltration of binder into a powder stacking.
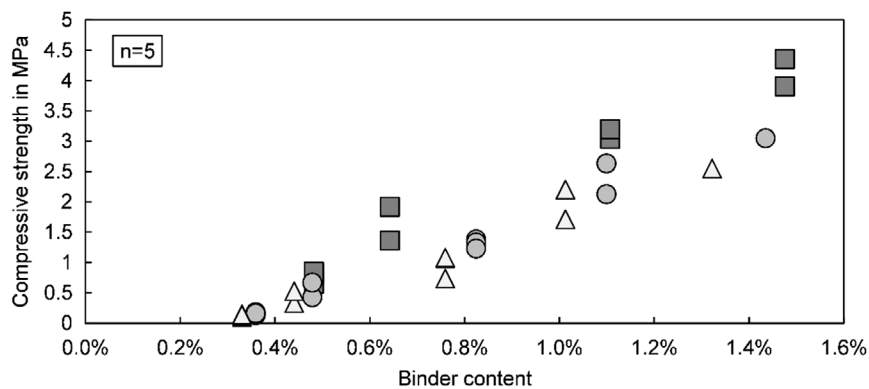
Figure 11. Development of average compressive strength ($n = 5$) with increasing binder contents at layer thicknesses of 350, 470, and 510 μm.

The systematic differences between the specimens printed in patterns with stripes of vertical alignment show an influence of the recoating process on the mechanical properties. Vice versa, it proposes additional importance to adjusting the (currently typically fixed) resolution parameters in industrial 3D printing machines and positioning parts in the building volume. It is suspected that the roller's compressive force (that is applied perpendicular to the recoating direction) in conjunction with the movement results in shear forces that may loosen noncured binder bridges under unfavorable droplet arrangements. Further investigations on the directionality exceed the scope of this work but are recommended for future research.
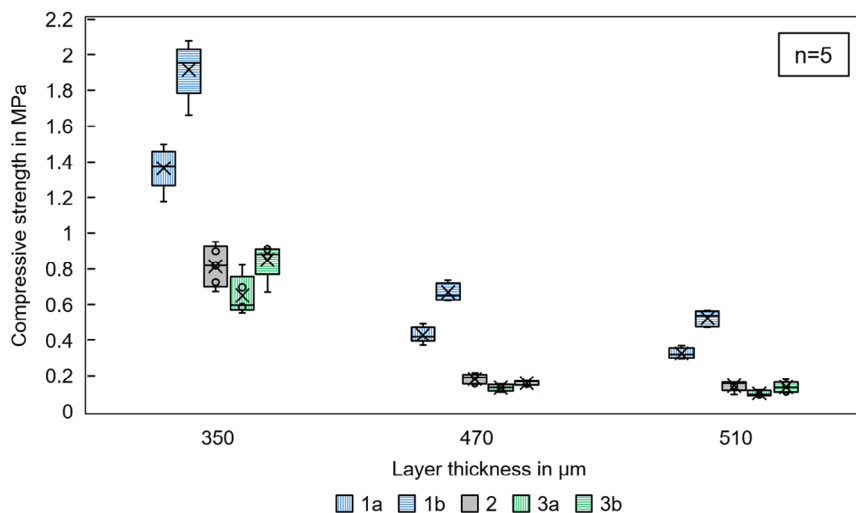
**ADVANCED
SCIENCE NEWS**

www.advancedsciencenews.com

**ADVANCED
ENGINEERING
MATERIALS**

www.aem-journal.com

Figure 12. Compressive strength of specimens ($n = 5$) printed with different droplet patterns for three levels of layer thicknesses.
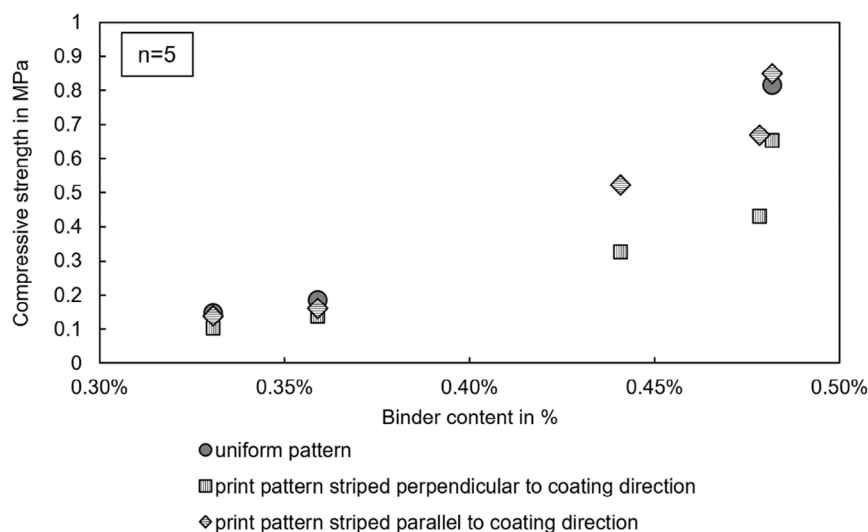

Figure 13. Compressive strength of specimens ($n = 5$) printed with different droplet patterns as a function of the binder content.

5.2. Infiltration Analysis

Herein, the infiltration behavior when applying the same printing patterns in simulation experiments is further investigated without a distinction between the orientations of the patterns to the recoating direction (*a* and *b*). For this reason, the patterns no. 1 and 3 are not differentiated into variants *a* and *b* in the diagrams relating to the simulation (**Figure 14–19**). Three simulations are conducted for each pattern using randomly generated RVEs of the same size.

The progression of infiltration depth over time is presented in Figure 14. The binder impact and spreading kinematic phase ends after ≈50 ms at the latest. Afterward, capillary forces take over and gradually drive further permeation into the powder bed. Infiltration is shown to propagate in a gradual manner from a particle–particle contact next to the location of droplet impact

to deeper locations where binder bridges form within milliseconds to seconds after the droplets' arrival.

The infiltration depth of droplet pattern no. 3, exhibiting the lower proportion of total ejected binder in relation to the printed area and the maximum droplet spacing in one direction (Table 1), tends to be lower than the alternative patterns applied in this study. A distinction from pattern no. 2 (which has the same total binder amount like pattern no. 3 but a homogeneous droplet spacing in *x*- and *y*-direction) is observed. In particular, the discrepancy between the three simulations is higher for the simulations relating to the striped droplet patterns no. 1 and no. 3. This effect is attributed to the fact that the RVE for pattern no. 2 is equilateral whereas those for the patterns no. 1 and 3 are different in width and length. The flow fronts of patterns no. 1 and 2 advance in a similar manner. This is quite remarkable, given that pattern no. 1 (which has the double droplet spacing in
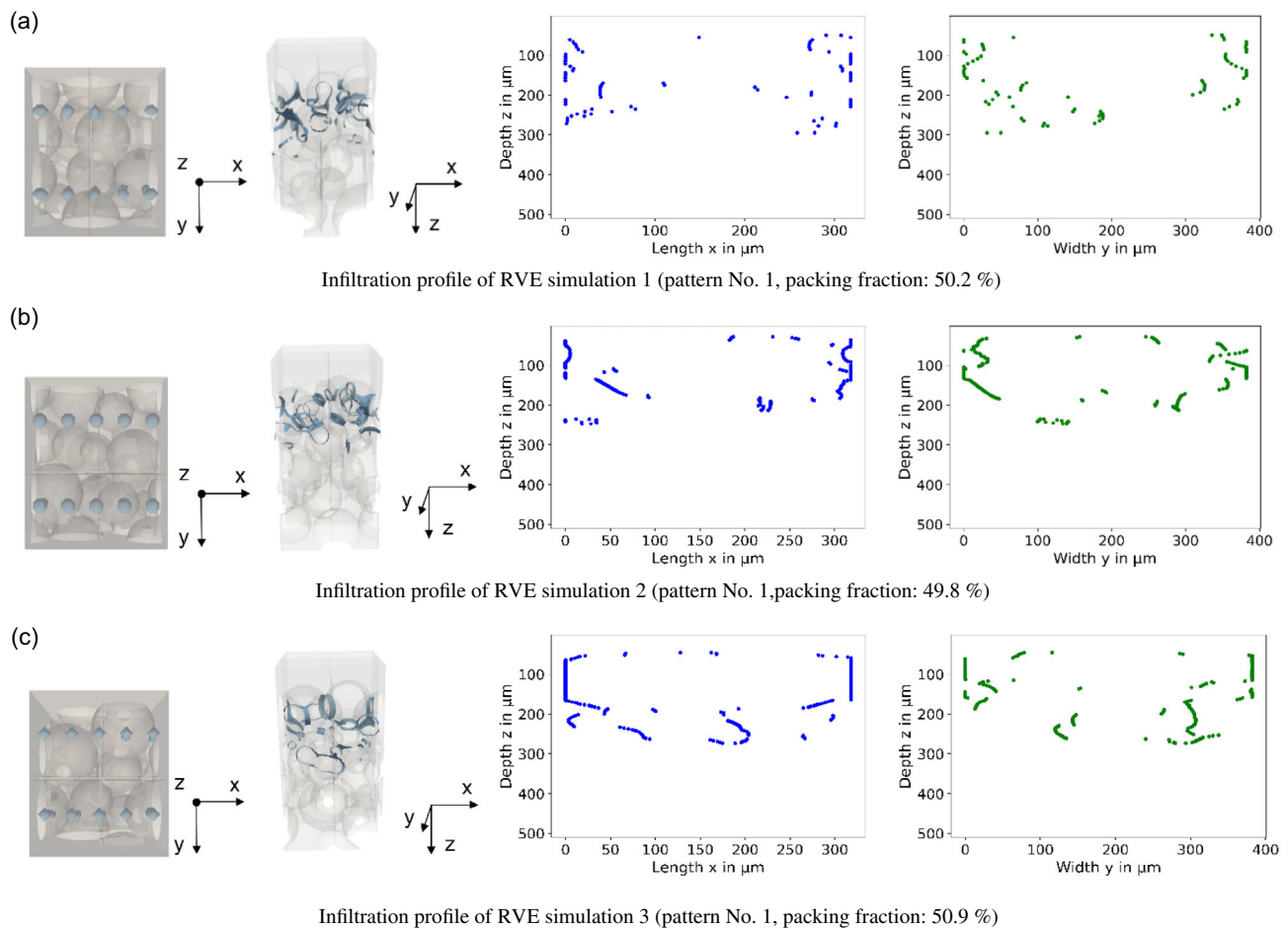
2300212 (12 of 20)
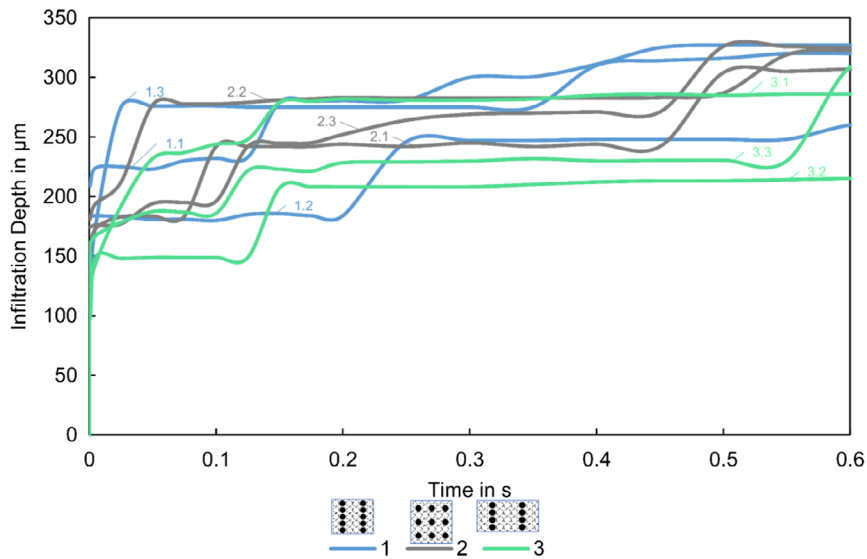
Figure 14. Progression of the infiltration depth over time for three simulations of each droplet pattern on different RVEs. The infiltration depth represents the maximum extension of binder fluid (volume fraction $\alpha = 0.5$) in z-direction.
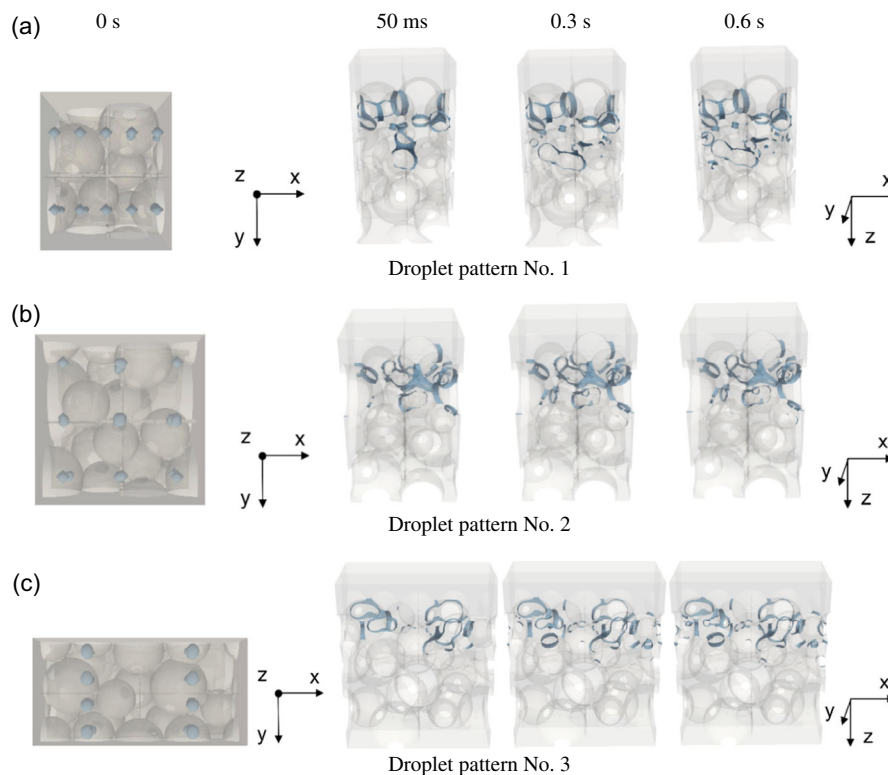
Figure 15. Microstructural infiltration of the binder at certain simulation timesteps after ejection. Left: top view on RVE and droplet positions; right: side view of infiltrated RVE at different time steps. Illustration of the infiltration progress for a) droplet pattern No. 1, b) No. 2, and c) No. 3.

y- compared to x-direction) comes with a one-third higher total binder amount. For a detailed analysis, a visualization of the infiltrated microstructure and the infiltration profiles at the timesteps of 50 ms (considered as the end of the kinematic phase), 0.3 s (considered as a representative time for taking capillary action into account), and 0.6 s (the end of the simulation) are shown and interpreted in the following subsection. However, the high spread within the results indicates the need for a greater number of simulations to account for a statistically significant behavior of a powder bed in binder jetting.

ADVANCED
SCIENCE NEWS
www.advancedsciencenews.com

ADVANCED
ENGINEERING
MATERIALS
www.aem-journal.com

(a)

Infiltration profile of RVE simulation 1 (pattern No. 1, packing fraction: 50.2 %)

(b)

Infiltration profile of RVE simulation 2 (pattern No. 1,packing fraction: 49.8 %)

(c)

Infiltration profile of RVE simulation 3 (pattern No. 1, packing fraction: 50.9 %)

Figure 16. Illustration of the infiltration profiles of droplet pattern no. 1 on three different randomly generated powder bulks 0.3 s after ejection. Simulation 2 b) shows a comparatively larger number of small particles located in the uppermost infiltrated volume. Coincidently, a significantly lower infiltration depth is observed in this simulation. a) Infiltration profile of RVE simulation 1 (pattern no. 1, packing fraction: 50.2%). b) Infiltration profile of RVE simulation 2 (pattern no. 1,packing fraction: 49.8%). c) Infiltration profile of RVE simulation 3 (pattern no. 1, packing fraction: 50.9%).
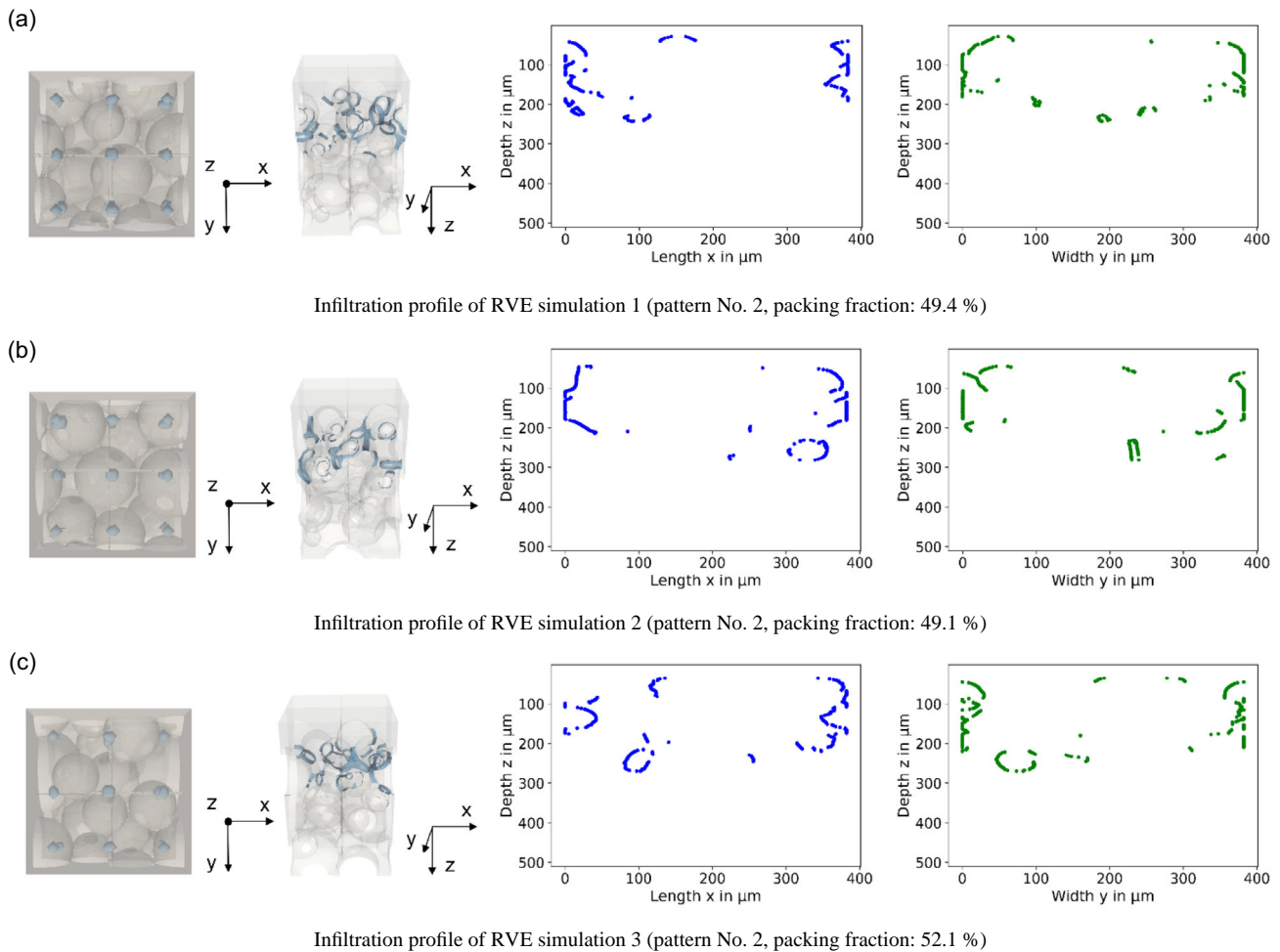
5.2.1. Microstructural Analysis

The infiltration of binder into a porous powder bed is visualized utilizing three simulations (Figure 15) that show an approximately identical packing fraction (average 51.3% at a tolerance of 0.4%). At 50 ms, the binder flow front already reaches the second row of particles in the z-direction. (The particles are not arranged in layer-wise uniformity but in a random distribution in all directions. For convenience, the particle location in z-direction is evaluated using the term "second row" or "third row" for all particles allocated roughly in a z-distance of one or two mean particle sizes from the uppermost particles, respectively.). Moreover, the powder bulks infiltrated by the striped patterns no. 1 and 3 clearly show fragmentary infiltration in the x–y-plane visible by not yet formed binder bridges in the uppermost areas close to the printhead. The binder microstructure at a time of 0.3 and 0.6 s after ejection is very similar, apart from minor isolated binder bridges. Across all nine simulations conducted herein, only two show the further formation of those minor bridges in the third row of particles in the z-direction at 0.6 s (Figure 15b).

Scheel et al. investigated the shape of liquid clusters via 3D X-ray microtomography and categorized them by their number of interfaces. With increasing liquid volume proportions, single isolated capillary bridges were found to transform into larger clusters termed trimer, pentamer, and larger formations.[47] According to this classification, primarily isolated capillary bridges and trimers which can coalesce from three capillary bridges located at a triangular configuration of particles were found to form in the present arrangements of spherical grains.

5.2.2. Analysis of Infiltration Profiles

Figure 16 visualizes the infiltration of three different, randomly generated RVEs with droplet pattern no. 1. The respective powder packing fraction is calculated automatically and returned by the software.

The profiles are generated by automatically analyzing the minimum and maximum liquid extent as described above. In pattern no. 1, the droplet distance in the y- is triple the distance in the x-direction. The majority of particles of the sand system GS14 RP are 125–180 μm in diameter.[24] Pattern no. 1's y-resolution is

ADVANCED
SCIENCE NEWS
www.advancedsciencenews.com

ADVANCED
ENGINEERING
MATERIALS
www.aem-journal.com

(a)

Infiltration profile of RVE simulation 1 (pattern No. 2, packing fraction: 49.4 %)

(b)

Infiltration profile of RVE simulation 2 (pattern No. 2, packing fraction: 49.1 %)

(c)

Infiltration profile of RVE simulation 3 (pattern No. 2, packing fraction: 52.1 %)

Figure 17. Illustration of the infiltration profiles of droplet pattern no. 2 (equidistant droplets) on three different randomly generated powder bulks 0.3 s after ejection. Homogeneous infiltration profiles are observed in all three RVE samples. a) Infiltration profile of RVE simulation 1 (pattern no. 2, packing fraction: 49.4%). b) Infiltration profile of RVE simulation 2 (pattern no. 2, packing fraction: 49.1%). c) Infiltration profile of RVE simulation 3 (pattern no. 2, packing fraction: 52.1%).

191.25 μm. Thus, in randomly distributed powder bulks of this PSD, there is a high probability of a minor influence of the striped pattern on the infiltration profile. Figure 16 shows necking in the y-direction in the lower regions of the powder bed (from $\approx z = 200$ μm). Since the distance between two droplets in y-direction is as high as 255 μm, whereas an average sand grain measures only 135 μm, a high probability for fragmentary infiltration is observed. The two rows of proximate droplets tend to converge to a single-flow front. Moreover, Figure 16b evidences the influence of the powder's distribution within the RVE on the infiltration profile. Coincidently, the RVE of simulation 2 exhibits a more fine-grained structure in the uppermost region. A lower infiltration is observed in this case. This is believed to be due to an increased binder consumption of those particles that show a higher surface-to-volume proportion. The average absolute infiltration depth from those profiles can be estimated to about 250 μm.
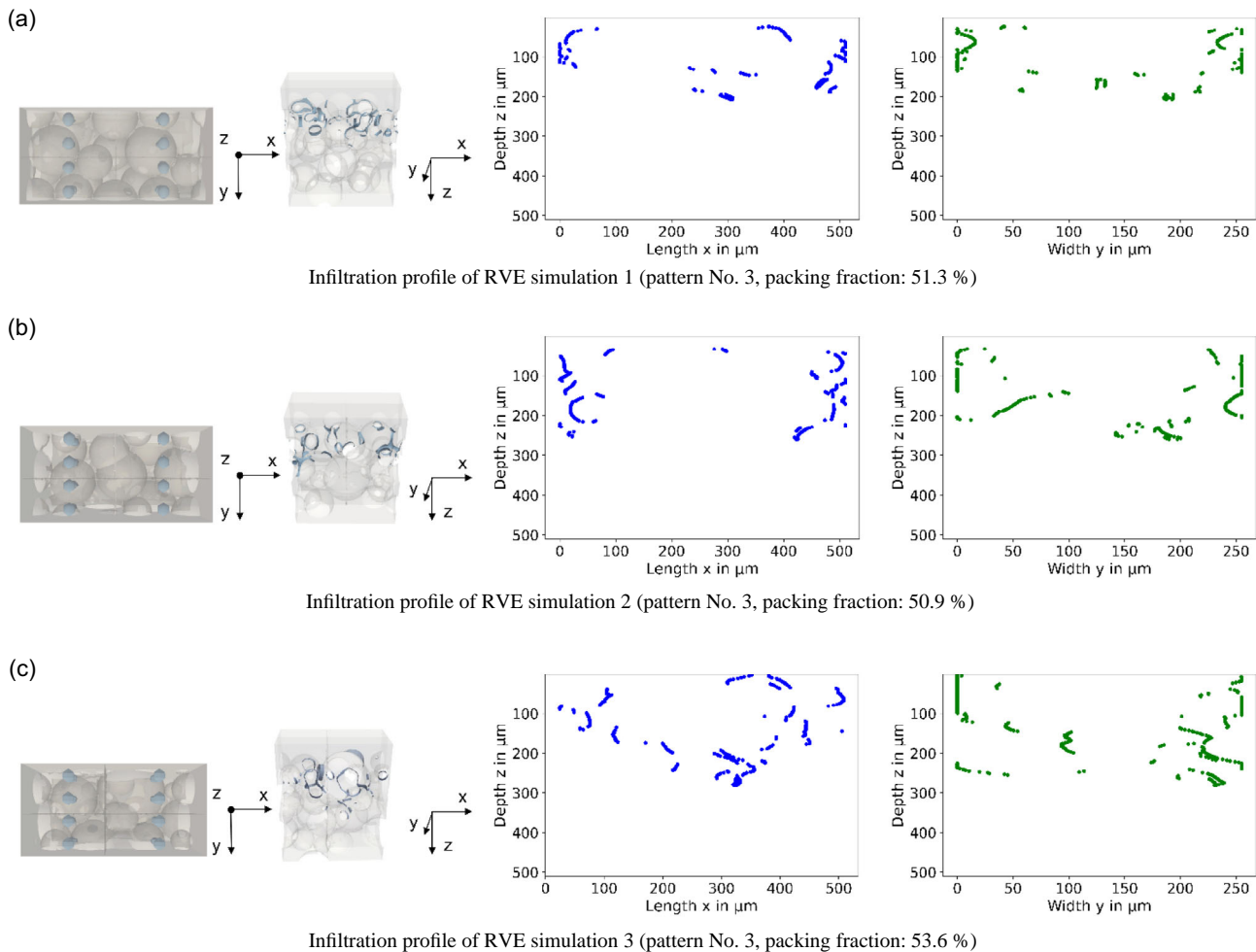
Similarly, Figure 17 visualizes the infiltration profiles occurring with droplet pattern no. 2 on other randomly generated powder bulks. The droplets' distance in pattern no. 2 is uniform

in x and y. No considerable necking in the z-direction is observed. Only individual binder bridges are found below a relatively homogeneous infiltration level. The average absolute infiltration depth from those profiles is about 220 μm.

Pattern no. 3 shows the most inhomogeneous droplet ejection with a fourfold increase in resolution in one direction than the other, in other words, a distance between two droplets of 255 μm, which is larger than the average particle size of the material used. Similar to Figure 16b and **18**a a significantly lower infiltration depth which can be attributed to the higher proportion of small particles in this randomly generated RVE is shown. Figure 18c evidences the effect of the local microscopic powder distribution: coincidently, multiple droplets impinge on one large particle, resulting in a local distribution of a major fraction of binder around this particle.

5.2.3. Analysis of the Volume Proportion Infiltrated by Binder

To verify the estimations on infiltration depth from the infiltration profiles and for automation purposes, the maximum volume

(a)

Infiltration profile of RVE simulation 1 (pattern No. 3, packing fraction: 51.3 %)

(b)

Infiltration profile of RVE simulation 2 (pattern No. 3, packing fraction: 50.9 %)

(c)

Infiltration profile of RVE simulation 3 (pattern No. 3, packing fraction: 53.6 %)

Figure 18. Illustration of the infiltration profiles of droplet pattern no. 3 on three different randomly generated powder bulks 0.3 s after ejection. Simulation 1 a) shows a higher number of binder bridges in the upper region and a lower overall infiltration depth. Simulation 3 c) visualizes the crucial influence of the powder bed's microscopic nature on infiltration behavior: multiple droplets hit one bigger particle, merge, and disperse around this particle a) Infiltration profile of RVE simulation 1 (pattern no. 3, packing fraction: 51.3%); b) infiltration profile of RVE simulation 2 (pattern no. 3, packing fraction: 50.9%); c) infiltration profile of RVE simulation 3 (pattern no. 3, packing fraction: 53.6%).

coverage of the binder is calculated considering the respective RVE packing fraction and the maximum spread of liquid determined in 2 μm slices and displayed in Figure 19.

The volume proportion infiltrated by binder, hereinafter referred to as "infiltrated volume", of 100% means an occurrence of binder exactly on the borders of the RVE volume in the x- and y-direction. This method is considered a first attempt to automatically determine the infiltration depth contributing to strength. However, it goes with several uncertainties and needs to be further elaborated: inner gaps within the infiltrated volume cannot be determined. Moreover, no statement can be made in regard to the local saturation with binder, the size, or the strength of binder bridges. Only droplet pattern no. 2 (Figure 19b) shows consistent results for all three sample simulations. Here, the infiltrated volume rapidly declines from 200 to 250 μm. The courses of the simulations of droplet pattern no. 1 (Figure 19a) vary widely but show a steady tendency of a slight decrease from 150 μm depth to a depth of 280 μm.

The courses of the samples of droplet pattern no. 3 (Figure 19c) are similar to pattern no. 1 but, within the simulations, significantly deviating and thus hard to interpret.

5.3. Discussion

The simulation methods and results shown above demonstrate the CFD tool's adequacy for the analysis of binder infiltration in randomly generated spherical powder bulks from designated PSDs.

Since cyclic boundary conditions are applied to the surrounding faces of the RVE, the automated data analysis methods still need to be applied with care. This is because a binder bridge randomly located directly on the outer edge automatically leads to a localization of binder in both RVE limits in this direction and mistakenly 100% infiltrated volume.

Those methods already enabled multiple observations valuable for future developments in binder jetting technology: a
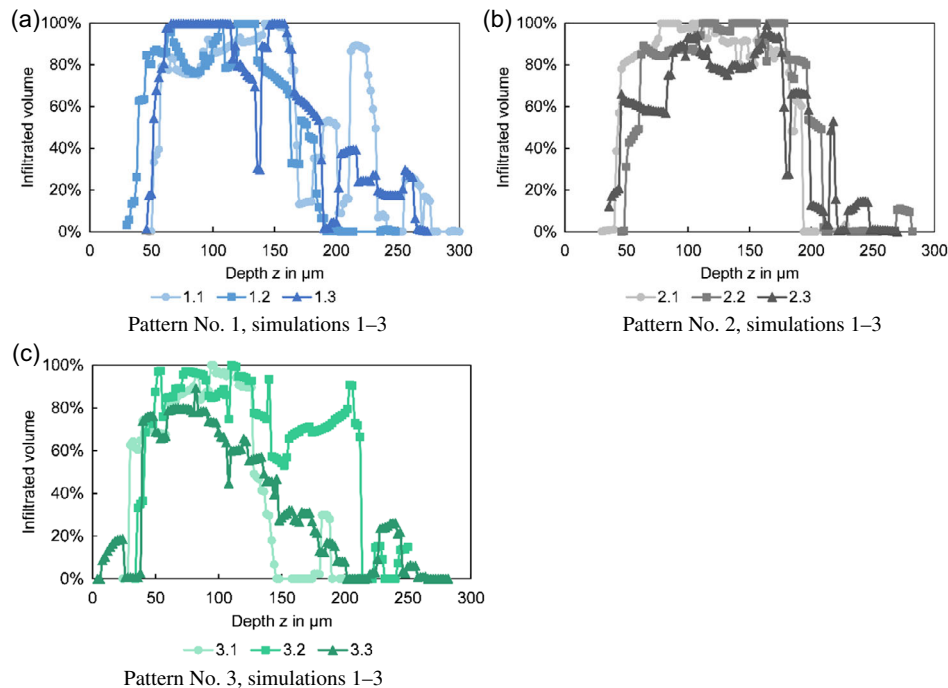
Figure 19. Automated calculation of the volume proportion infiltrated by binder using droplet pattern a) no. 1, b) no. 2, and c) no. 3 over the infiltration depth z in each simulation case. An equal resolution in x and y (b) results in similar infiltration profiles for different RVEs, while the variation in the simulated infiltration depth varies widely for the striped patterns (a) and (c).

simulation time of 0.3 s after ejection can be considered suitable for comparative analysis of binder infiltration profiles. Only minor, negligible liquid flow can be observed after 0.3 s. Since the simulation time is decisive regarding the required computing resources, this knowledge facilitates further investigations. Moreover, crucial influence of the particle sizes on the location of droplet impact is indicated. A more significant proportion of smaller particles occurring in the x–y-plane lead to an impeded infiltration in the z-direction. In contrast, an individual big particle hit by multiple droplets can direct coalescing droplets to its particle contacts and thus promote uneven vertical infiltration. The structure of the powder bulk and its position relatively to the droplet impact locations determine the binder infiltration depth. Statistical effects related to the macroscopic powder bulk generation (influenced by, e.g., recoating) are considered decisive. Binder infiltration depth may be improved by increasing the number of droplets that are ejected above valley-like regions of the powder bed's surface topography. Smoothening and compacting the freshly applied layer during recoating may be detrimental to promoting binder infiltration. Roughening the powder topography might be beneficial. Increasingly irregular infiltration profiles are observed at significantly uneven inkjet resolutions in x and y. Droplet coalescence may exhibit a preferred direction if the distance between droplets in one direction is much higher than in the other direction. The infiltration profiles give a first indication of the infiltration depth of the binder using the three different droplet patterns. As expected, the higher binder content applied using pattern no. 1 leads to the deepest infiltration on average, $\approx 30\,\mu m$ deeper infiltration compared to the alternative droplet patterns exhibiting a lower binder proportion.

The high-speed camera observations conducted herein confirm that binder infiltration in inkjet printing takes place around a few hundreds of milliseconds, whereby the strongest kinetics can be observed in the first 20 ms.

For putting the observations into context with the compressive strength values attained in experiments, additional considerations have to be conducted. The infiltration depth is not to be confused with the resulting layer thickness linkable to the previous layer. For an estimation of the highest attachable layer thickness from the simulation results it has to be considered that the binder fixes particles on the bottom frontier of the infiltration depth. Thus the layer thickness attachable to the previous layer is the infiltration depth plus the bound particles.

Their particle sizes and the spatial location of their bond are statistically distributed. **Figure 20** shows an unimodal conceptual model distinguishing between vertical, horizontal, and inclined bonds between particles. Imagining the bond displayed represents the lowest binder bridge observed in the simulation, the distance to be covered beyond the infiltration depth is dependent on the binder bridge's orientation and the grain sizes. Thinking in terms of probabilities and quantities, vertical bonds (left) is rare but potentially capable of generating a comparatively long-distance effect ($2r$) while horizontal bonds (middle) may occur along a grain's circumference but only impact particles in the same depth and have a depth effect of only the radius r. However, the most probable scenario is the inclined bond (right) that may occur throughout the grain's hemispherical area in different angles β.

In simplified terms, the effect depth can be calculated to $r(1+\cos\beta)$. 45° may be the most relevant angle. Transferred to
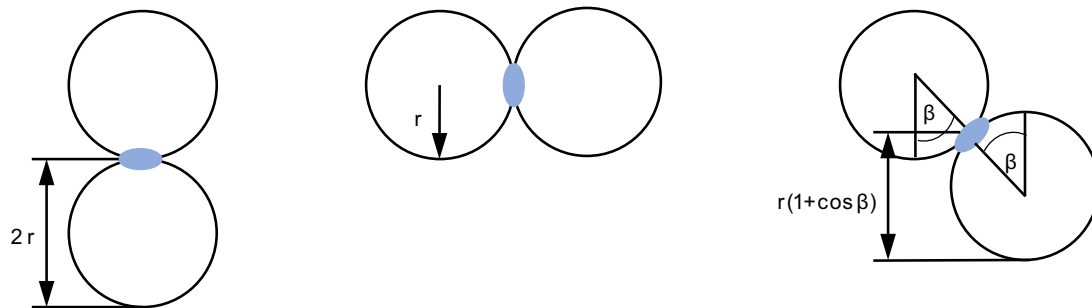
Figure 20. Conceptual unimodal model visualizing the bonds between particles at the lowest point within a RVE. Left: vertical bond. Middle: horizontal bond. Right: inclined bond.

the material investigated herein, one can estimate the most probable bonding effect emerging at the lowest point in an infiltration volume to the medium grain size radius times (1+cos45°) which is 115 μm. The average infiltration depth found in the simulation is 250 μm using droplet pattern no. 1. Here, a reliable effect of bonding (45°) is expected for layer thicknesses up to 365 μm. In long distance, effects through vertical bondings might be present until a layer thickness reaches the maximum infiltration depth of 300 μm plus one additional grain which might be as large as 250 μm, resulting in a deployable layer thickness of 550 μm, and in average 135 μm resulting in a thickness of 485 μm. Strength testing here reveals compressive strength above 1 MPa for those specimens printed with a layer thickness of 350 μm and significantly less strength at a layer thickness of 470 or 510 μm.

For droplet no. 2, simulation reports infiltration depths around 220 μm. Following the proposed simplified calculation, this would lead to reliable bonding of layers up to 335 μm which is out of the investigated range. Bonding is estimated to exist until 530 μm here following the same strategy of determination. The experiments showed compressive strengths of around 0.8 MPa at 350 μm and below 0.2 MPa for thicker layers.

Following this hypothesis, it can be assumed that residual strength may be anticipated when combining infiltration profile analysis from simulation and material-related statistics. However, only strength values above 1 MPa are considered relevant for enabling secure handling and further mechanisms that were not part of this investigation might additionally influence the specimens' strength. The dramatic decline in strength with thicker layers for industrially relevant binder proportions should be part of future simulation studies and experimental investigations to prove evidence on the conceptual model. Statistics will provide information on contribution factors in infiltration behavior and strength development.

Apart from this, the following aspects could have an additional influence. 1) In this study, no attention is paid to the chemical reaction that produces water during polycondensation. The reaction products may coalesce with the binder and promote further infiltration. 2) Evaporation of binder mass due to reaction kinetics is not taken into account. Further transport mechanisms may enable the formation of binder bridges at a larger distance within a longer time period than the observed. 3) Fluid flow is still preceding after the simulation time even if very slow, capillary action may promote further infiltration. 4) Capillary forces drop off quickly[48] in microstructural gaps. A more realistic particle morphology may be investigated in the future. 5) The homogeneous wetting of the powder bulk may have a greater influence on infiltration than expected. Instead of activator fluid deposition analogous to binder ejection, appropriate parameters may be assigned to the powder bulk to account for wetting all over the RVEs.

In order to take these potential influences into account in modeling, additional boundary conditions, some of which go beyond the state of the art or demand for resource-intensive further studies, need to be established.

Moreover, the experimental results surprisingly showed significantly improved strength at a certain orientation when using the irregular striped droplet pattern. A reconciliation with DEM recoating simulation and further experimental work may provide insight into the cause-and-effect chain. The interaction between layers is not in scope of this study. For getting a first imagination, one layer can be abstracted as the contingent of all particles in contact with binder. Each layer has a planarized surface due to the compilation of the RVE. Since the material can be handled, there must be binder bridges between the individual layers. In reality, layer formation during recoating is dependent on the properties of the previous layer, in particular on the wetting of surfaces by binder. The build-up of powder structures are subject to deviations in packing efficiency or grain orientations when comparing recoating on printed to nonprinted surfaces (increased cohesivity and decreased flowability). Such aspects need to be modeled in the future.

The simulation tools are ready for use in binder jetting process development tasks and will be utilized for identifying appropriate binder jetting parameters and suitable material systems for different applications. Especially the choice of a printhead type and the parameters can be adapted to a certain particle contingent using that tool. In addition, the powder can be optimized for special applications. Since prior studies showed the influence of the grain surface and shape[18] on binder infiltration, future advancements in the simulation setup should include the implementation of realistic grain morphologies. Due to the high impact of the local particle structure, investigations on a higher number of representative RVE structures and alternative binder jetting parameters will be of further interest.

**ADVANCED
SCIENCE NEWS**

www.advancedsciencenews.com

**ADVANCED
ENGINEERING
MATERIALS**

www.aem-journal.com

6. Conclusion

This article proposes a CFD approach to simulate binder infiltration in 3D printing. A method for randomly generating RVEs of a designated PSD has been introduced, as well as several approaches in automated analysis of the infiltration profile and infiltrated volume. It was demonstrated that the simulation approach is a valuable tool to indicate the influencing factors of binder infiltration in porous powder bulks and propose new strategies for application-tailored material and process developments.

In a first application study, those methods were applied to investigate binder infiltration using different droplet spacings or resolutions in the x- and y-direction. A crucial influence of particle sizes appearing at the exact location of droplet impact (beyond the global PSD) has been evidenced. A high fines content in the impact zone resulted in an impeded infiltration in the z-direction. In contrast, individual particles of higher diameter that are hit by multiple droplets can promote the coalescence of droplets and highly localized vertical infiltration by driving the merged droplets along their outline. Moreover, the results indicate that improved infiltration depths are conceivable when occasionally encountering valley regions of the powder's surface topography. The proposed analysis tools can already indicate the infiltration profile of the binder using the three different droplet patterns, but they need to be refined for detailed analyses. To account for the behavior of a macroscopic powder bed comprising multiple randomly arranged particle arrangements, it is suggested to simulate a higher number of randomly generated RVEs.

The experimental results showed significantly improved strength using uniform droplet patterns or patterns striped parallel to the recoating direction and, thus, a directional dependency of strength in the build volume. At this low-binder droplet mass and high-droplet spacing applied in this study, an average infiltration of 250 μm was found in the simulation which is presumed to achieve reliable bonding for layer thicknesses up to 365 μm. Still, the specimens produced experimentally showed a measurable, although low, strength even at a layer thickness of 510 μm. This indicates the decisiveness of statistics in respect to the arrangement of particles in accordance with the powder's PSD, or the presence of further interferences, for example, binder chemistry, powder morphology, or wetting.

The simulation approach proved suitable for the investigation of powder–binder interaction. In the first step, the simulation setup was introduced and applied to an exemplary use case. The plausibility of the simulation was fundamentally tested by comparing the infiltration kinetics derived from the simulation to high-speed camera observations.

Future studies will address a comprehensive experimental validation to verify the agreement between the visualization and microstructural effects. Further advancements in the simulation will include the implementation of angular grain morphologies and different particle surface properties.

Acknowledgements

Conflict of Interest

The authors declare no conflict of interest.

Data Availability Statement

The data that support the findings of this study are available from the corresponding author upon reasonable request.

Keywords

[1] Deutsches Institut für Normung e.V., *DIN EN ISO/ASTM 52900: Additive Manufacturing - General Principles - Fundamentals and Vocabulary*, Beuth Verlag GmbH, Berlin **2017**.

[2] D. Günther, P. Erhard, S. Schwab, I. Taha, *Materials* **2021**, *14*, 4639.

[3] J. Kang, Q. Ma, *China Foundry* **2017**, *14*, 157.

[4] GE, GE Renewable Energy, Fraunhofer IGCV, and voxeljet AG plan to develop world's largest sand binder jetting 3D printer for offshore wind turbines | GE News, **2021**, https://www.ge.com/news/press-releases/ge-renewable-energy-fraunhofer-igcv-voxeljet-plan-develop-world-largest-sand-binder-jetting-3D-printer-offshore-wind-turbines (accessed: December 2022).

[5] A. Mostafaei, A. M. Elliott, J. E. Barnes, F. Li, W. Tan, C. L. Cramer, P. Nandwana, M. Chmielus, *Prog. Mater. Sci.* **2020**, *40*, 100707.

[6] A. P. Clares, G. Manogharan, in *ASME 2021 16th Int. Manufacturing Science and Engineering Conf.*, online/virtual **2021**, https://doi.org/10.1115/MSEC2021-63351.

[7] Y. Lee, P. Nandwana, S. Simunovic, *Prog. Addit. Manuf.* **2022**, *7*, 111.

[8] G. Miao, W. Du, Z. Pei, C. Ma, in *ASME 2019 14th Int. Manufacturing Science and Engineering Conf.*, Erie, PA, USA **2019**, https://doi.org/10.1115/MSEC2019-2925.

[9] Y. Wang, P. Jia, W. Yang, K. Peng, S. Zhang, *Mod. Phys. Lett. B* **2018**, *32*, 1850272.

[10] X. Gao, W. Yang, H. Xian, X. Tu, Y. Wang, *CMES* **2020**, *124*, 227.

[11] H. Deng, Y. Huang, Y. Yang, S. Wu, Z. Chen, *MATEC Web Conf.* **2022**, *355*, 1009.

[12] T. Colton, N. B. Crane, *Addit. Manuf.* **2021**, *37*, 101711.

[13] F. Fu, P. Li, K. Wang, R. Wu, *Langmuir* **2019**, *35*, 2917.

[14] X.-P. Li, Y.-E. Wang, A. Ahmed, Q.-H. Wei, Y. Guo, K. Zhang, Y.-K. Shi, *Appl. Sci.* **2022**, *12*, 1898.

[15] H. Tan, *Chem. Eng. Sci.* **2016**, *153*, 93.

[16] J. J. Wagner, C. Fred Higgs, *J. Tribol.* **2021**, *143*, 051113.

[17] S. Barui, H. Ding, Z. Wang, H. Zhao, S. Marathe, W. Mirihanage, B. Basu, B. Derby, *ACS Appl. Mater. Interfaces* **2020**, *12*, 34254.

[18] S.-Y. Chun, T. Kim, B. Ye, B. Jeong, M. Lee, D. H. Lee, E.-S. Kim, H. Lee, H.-D. Kim, *Appl. Surf. Sci.* **2020**, *515*, 145979.

[19] N. D. Parab, J. E. Barnes, C. Zhao, R. W. Cunningham, K. Fezzaa, A. D. Rollett, T. Sun, *Sci. Rep.* **2019**, *9*, 2499.

[20] A. U. Rehman, K. Azher, A. Ullah, C. S. Tüfekci, M. U. Salamci, *Rapid Prototyping J.* **2023**, *29*, 1499.

[21] Y.-L. Cheng, Y.-T. Li, Y.-T. Yang, K.-T. Tang, F.-A. Jhuang, K.-H. Li, C.-W. Lu, *Addit. Manuf.* **2022**, *56*, 102929.

[22] C. Hartmann, L. van den Bosch, J. Spiegel, D. Rumschöttel, D. Günther, *Materials* **2022**, *15*, 3798.

[23] OpenCFD Limited, *OpenFOAM Programmer's Guide: Version V1912*, OpenCFD Ltd., Bracknell, UK **2019**, https://doc.openfoam.com/ (accessed: July 2022).

[24] Strobel Quarzsand GmbH, GS14 RP, **2022**, https://www.strobel-quarzsand.de/media/GS14RP.pdf (accessed: January 2023).

[25] GIMP, GNU Image Manipulation Program, **2023**, https://docs.gimp.org/2.10/en/ (accessed: January 2023).

[26] I. Budavári, G. Gyarmati, L. Varga, *Int. J. Metalcast.* **2022**, *16*, 1415.

[27] OpenFOAM, User Guide, **2022**, https://www.openfoam.com/documentation/user-guide (accessed: December 2022).

[28] J. Brackbill, D. Kothe, C. Zemach, *J. Comput. Phys.* **1992**, *100*, 335.

[29] M. J. Nieves-Remacha, L. Yang, K. F. Jensen, *Ind. Eng. Chem. Res.* **2015**, *54*, 6649.

[30] *A Survey of Interface Tracking Methods in Multi-Phase Fluid Visualization* (Eds: F. Chen, H. Hagen), Schloss Dagstuhl - Leibniz-Zentrum fuer Informatik GmbH, Wadern/Saarbruecken, Germany **2011**.

[31] R. Hill, *J. Mech. Phys. Solids* **1963**, *11*, 357.

[32] C. Pelissou, J. Baccou, Y. Monerie, F. Perales, *Int. J. Solids Struct.* **2009**, *46*, 2842.

[33] J. Zhou, Y. Zhang, J. K. Chen, *J. Manuf. Sci. Eng.* **2009**, *131*, 031004.

[34] J. W. Eaton, D. Bateman, S. Hauberg, R. Wehbring, *GNU Octave Version 6.1.0 Manual: A High-Level Interactive Language for Numerical Computations* **2020**, https://www.gnu.org/software/octave/doc/v6.1.0/ (accessed: August 2022).

[35] C. Geuzaine, J.-F. Remacle, *Int. J. Numer. Methods Eng.* **2009**, *79*, 1309.

[36] H. Miyanaji, M. Orth, J. M. Akbar, L. Yang, *Front. Mech. Eng.* **2018**, *13*, 504.

[37] M. Scheel, *Doctoral Thesis*, University of Göttingen, Göttingen **2009**.

[38] Y. Wang, R. Yu, S. Yin, R. Tan, Y. Lou, *China Foundry* **2021**, *18*, 581.

[39] Kitware, Inc., *ParaView's Python Documentation: Version 5.9.0*, **2022**, https://kitware.github.io/paraview-docs/v5.9.0/python/ (accessed: December 2022).

[40] C. A. Schneider, W. S. Rasband, K. W. Eliceiri, *Nat. Methods* **2012**, *9*, 671.

[41] G. Onoda, *J. Am. Ceram. Soc.* **1976**, *59*, 236.

[42] S. I. Yanez-Sanchez, M. D. Lennox, D. Therriault, B. D. Favis, J. R. Tavares, *Ind. Eng. Chem. Res.* **2021**, *60*, 15162.

[43] S. Diener, A. Zocca, J. Günster, *Open Ceram.* **2021**, *8*, 100191.

[44] M. Vaezi, C. K. Chua, *Int. J. Adv. Manuf. Technol.* **2011**, *53*, 275.

[45] K. P. Hapgood, J. D. Litster, S. R. Biggs, T. Howes, *J. Colloid Interface Sci.* **2002**, *253*, 353.

[46] Y. Mao, J. Li, W. Li, D. Cai, Q. Wei, *J. Mater. Process. Technol.* **2021**, *291*, 117020.

[47] M. Scheel, R. Seemann, M. Brinkmann, M. Di Michiel, A. Sheppard, S. Herminghaus, *J. Phys.: Condens. Matter* **2008**, *20*, 494236.

[48] M. Scheel, R. Seemann, M. Brinkmann, M. Di Michiel, A. Sheppard, B. Breidenbach, S. Herminghaus, *Nat. Mater.* **2008**, *7*, 189.